arXiv:1301.1628v1 [physics.optics] 8 Jan 2013

Second harmonic generation in metal nano-spheres: full-wave analytical solution with both local-surface and nonlocal-bulk nonlinear sources

Antonio Capretti,[1, 2] Carlo Forestiere,[1, 2] Luca Dal Negro,[2] and Giovanni Miano[1, *]
[1] *Department of Electrical Engineering and Information Technology, Università degli Studi di Napoli Federico II, Via Claudio 21, 80125 Napoli, Italy*
[2] *Department of Electrical and Computer Engineering & Photonics Center, Boston University, 8 Saint Marys Street Boston, MA 02215, United States*

(Dated: January 9, 2013)

We present a full-wave analytical solution for the problem of second-harmonic generation from spherical particles made of lossy centrosymmetric materials. Both the local-surface and nonlocal-bulk nonlinear sources are included in the generation process, under the undepleted-pump approximation. The solution is derived in the framework of the Mie theory by expanding the pump field, the non-linear sources and the second-harmonic fields in series of spherical vector wave functions. We apply the proposed solution to the second-harmonic generation properties of noble metal nano-spheres as function of the polarization, the pump wavelength and the particle size. This approach provides a rigorous methodology to understand second-order optical processes in metal nanoparticles, and to design novel nanoplasmonic devices in the nonlinear regime.

PACS numbers: 42.65.Ky, 73.20.Mf, 78.35.+c, 78.67.Bf

I. INTRODUCTION

Nonlinear phenomena in metal nanostructures are gathering much attention due to their potential application as novel components for integrated optics.[1–4] Moreover, second harmonic (SH) generation from metal nanostructures provides a powerful tool for probing physical and chemical properties of material surfaces.[5,6] Noble metal nanoparticles support localized surface plasmons (LSPs). LSPs are collective oscillations of the conduction electrons, that strongly affect the optical response of the metal. When LSPs are resonantly excited, the local electromagnetic field is significantly enhanced in the particle, enabling the generation of nonlinear optical effects, such as harmonic generation, at relatively low excitation powers.

Second harmonic generation by nanoparticles originates from two contributions: the particle bulk and the surface contribution, respectively. In noble metal nanoparticles, the local-bulk source is absent because of the material centro-symmetry, and only the nonlocal-bulk contribution needs to be considered.[7] The local-surface contribution to SH radiation is due to the symmetry breaking at the interface with the embedding medium.[8,9] The magnitudes of the nonlocal-bulk and local-surface SH contributions depend on the shape of the nanoparticle and on the optical properties of the metal at the fundamental and second harmonic frequencies.[10,11]

Both the bulk and surface SH sources contribute significantly to the SH scattering response of a spherical nanoparticle, as already demonstrated in approximated analytical models developed to describe the SH generation from noble metal nanostructures with simple geometries, such as spheres and cylinders. In 1999, Dadap *et al.* studied the SH radiation generated from the surface of a sphere with radius R much smaller than the wavelength of the incident light λ ($2\pi R/\lambda << 1$, Rayleigh limit).[9] It is shown that the leading-order contributions to SH radiation arise from the electric-dipole $\mathbf{p}^{(2\omega)}$ and the electric-quadrupole $\overleftrightarrow{\mathbf{Q}}^{(2\omega)}$ moments, and the main selection rules for the SH scattering from a sphere are outlined. In Refs. 12 and 13, the Rayleigh limit is analyzed by taking into account both the bulk and the surfaces polarization sources, showing that the SH field is radiated by an effective electric dipole moment $\mathbf{p}_{eff}^{(2\omega)}(\hat{\mathbf{r}}) \cong \mathbf{p}^{(2\omega)} + i\, k_0 \overleftrightarrow{\mathbf{Q}}^{(2\omega)} \hat{\mathbf{r}}/3$ (the SH magnetic dipole emission is forbidden because of the axial symmetry of the system). It is demonstrated that both the nonlocal-bulk and the local-surface SH sources contribute to the induced electric dipole moment $\mathbf{p}^{(2\omega)}$, while only the local surface sources contribute to the induced electric quadrupole moment $\overleftrightarrow{\mathbf{Q}}^{(2\omega)}$, in the Rayleigh regime. The presence of distinct SH sources with their own radiation patterns causes the SH Rayleigh scattering process to differ significantly from the linear Rayleigh scattering. In particular, the theory predicts the absence of the SH signal in the forward direction and the $(k_0 R)^6$ scaling of the SH scattering cross-section.

The SH Rayleigh scattering model is inaccurate if the particle size is comparable with the wavelength, owing to the contributions of SH multipolar orders higher than 2 are not negligible. A full-wave analysis of the SH scattering from spherical particles of arbitrary size is developed in Ref. 14, but only the surface SH source was taken into account. Moreover, the enforced boundary conditions are incorrect,[7] resulting in zero SH radiation from the radial component of the source. Recently, a full wave theory of the SH radiation generated by a chain of parallel infinitely long cylinders, including both the bulk and surface nonlinear sources, has been developed in Ref. 4. A full-wave theory of the SH radiation generated in three-dimensional structures consisting of metallic spheres made of centro-symmetric materials has been proposed in Ref. 15, but here again the treatment is limited to the surface source.

In this paper we propose a full-wave analytical solution for the SH scattering from nano-spheres of arbitrary size, which includes both the contributions of the nonlocal-bulk and the local-surface SH sources. As a case of considerable interest, we apply this solution to investigate the SH radiation generated by noble metal nano-spheres. The present work is organized as follows. In Section II A the electromagnetic formulation of SH scattering by a metal nano-sphere is presented, and the analytical solution for the fields is defined, at both the pump and SH frequencies. In Section III the SH scattering from gold nano-spheres with increasing size is studied, as function of the wavelength and polarization of the pump field. In Section IV the conclusions are outlined. This manuscript is completed by six Appendices, where detailed formulas for the analytical calculation of all the quantities of interest are provided.

II. PROBLEM STATEMENT AND SOLUTION

A. Problem statement

Let us consider the electromagnetic field at frequency 2ω generated from a metal sphere of radius R, when illuminated by a time-harmonic electromagnetic plane-wave at frequency ω incoming from infinity. We use a spherical coordinate system (O, r, θ, ϕ) with the origin O in the center of the sphere, as in Fig. 1(a); we denote with $\left(\hat{\boldsymbol{r}}, \hat{\boldsymbol{\theta}}, \hat{\boldsymbol{\phi}}\right)$ the unit vectors of the spherical coordinate system. The domain of the electromagnetic field is the entire space $\mathbb{R}^3$, divided into the interior part of the metal domain $\dot{\Omega}_i$, the embedding medium $\dot{\Omega}_e$ and the metal surface Σ. The surface Σ is oriented in such a way that its normal $\hat{\mathbf{n}}$ points outward, $\hat{\mathbf{n}} = \hat{\mathbf{r}}\,|_{\Sigma}$. We use the convention $\mathbf{a}\left(\mathbf{r}, t\right) = Re\left\{\mathbf{A}^{(\Omega)}\left(\mathbf{r}\right)\exp\left(i\Omega t\right)\right\}$ for representing a time harmonic electromagnetic field at angular frequency Ω, where $\mathbf{r} = r\hat{\mathbf{r}}$. The second harmonic generation problem involves two electromagnetic fields oscillating at different frequencies: *the fundamental-frequency* electromagnetic field $\left(\mathbf{E}^{(\omega)}, \mathbf{H}^{(\omega)}\right)$ at frequency ω and the *second harmonic* electromagnetic field $\left(\mathbf{E}^{(2\omega)}, \mathbf{H}^{(2\omega)}\right)$ at frequency 2ω. We denote with $\left(\mathbf{E}_0^{(\omega)}, \mathbf{H}_0^{(\omega)}\right)$ the *incident (pump)* electromagnetic field:

$$\begin{aligned}\mathbf{E}_0^{(\omega)} &= E_0 e^{-i\mathbf{k}_0^{(\omega)}\cdot\mathbf{r}}\hat{\boldsymbol{\varepsilon}}_0 \\ \mathbf{H}_0^{(\omega)} &= \left(\frac{E_0}{\zeta_e}\right)\left(\hat{\mathbf{k}}_0 \times \hat{\boldsymbol{\varepsilon}}_0\right)e^{-i\mathbf{k}_0^{(\omega)}\cdot\mathbf{r}} \ ,\end{aligned} \tag{1}$$

where E_0 is the electric field magnitude of the linearly-polarized pump beam, $\hat{\boldsymbol{\varepsilon}}_{\mathbf{0}}$ is its polarization direction, $\hat{\mathbf{k}}_0$ its propagation direction, $\mathbf{k}_0^{(\omega)} = \hat{\mathbf{k}}_0 k_e(\omega)$, $k_e(\omega) = \omega\sqrt{\mu_e\varepsilon_e}$ and $\zeta_e = \sqrt{\mu_e/\varepsilon_e}$. The parameters ε_e and μ_e are the permittivity and the permeability of the embedding medium.

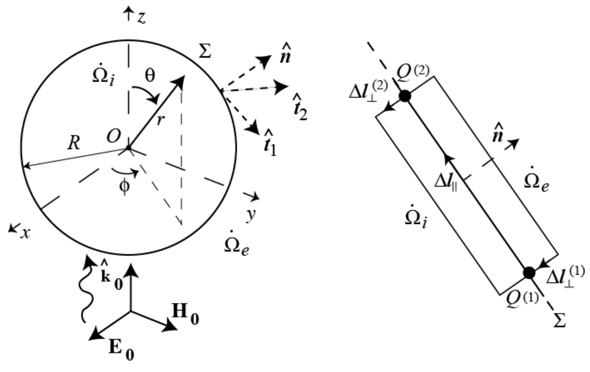

(a) (b)

FIG. 1. (a) Scheme of the spherical particle and coordinate system (O, r, θ, ϕ). (b) Elementary closed curve Δl across the *selvedge region* at the particle boundary.

Since the intensities of the SH fields generated by noble metals are always orders of magnitude weaker than the intensities of the pump fields, the SH fields do not significantly couple back to the fundamental fields (*undepleted-pump approximation*). As a result, the electromagnetic scattering problems at the fundamental frequency and at the SH frequency are both linear. The linear electromagnetic response of the metal is characterized, in the frequency domain, by the permittivity ε_i, which depends on the frequency, and by the permeability μ_i, that we assume independent of the frequency. The nonlinear optical response at SH frequency is phenomenologically described by a nonlinear polarization induced by the fundamental electric field $\mathbf{E}^{(\omega)}$. This polarization acts as the source of the SH electromagnetic radiation, and has both a local surface contribution $\mathbf{P}_s^{(2\omega)}$ defined on Σ and a nonlocal bulk contribution $\mathbf{P}_b^{(2\omega)}$ defined in $\dot{\Omega}_i$.[7,9]

Noble metals are centrosymmetric materials, therefore the leading term of the bulk nonlinear polarization density $\mathbf{P}_b^{(2\omega)}$ is given by:

$$\mathbf{P}_b^{(2\omega)} = \varepsilon_0 \overset{\leftrightarrow}{\chi}_b^{(2\omega)} \vdots \mathbf{E}^{(\omega)}\left(\nabla\mathbf{E}^{(\omega)}\right) \ \text{ in } \dot{\Omega}_i \ , \tag{2}$$

where $\overset{\leftrightarrow}{\chi}_b^{(2\omega)}$ is the quadrupolar contribution to the second-order nonlinear bulk susceptibility of the metal and ε_0 is the vacuum permittivity. Noble metals are also isotropic, therefore relation (2) becomes:

$$\begin{aligned}\mathbf{P}_b^{(2\omega)} =& \varepsilon_0\,\beta\mathbf{E}^{(\omega)}\nabla\cdot\mathbf{E}^{(\omega)} + \\ & \varepsilon_0\,\gamma\nabla\left(\mathbf{E}^{(\omega)}\cdot\mathbf{E}^{(\omega)}\right) + \varepsilon_0\,\delta'\left(\mathbf{E}^{(\omega)}\cdot\nabla\right)\mathbf{E}^{(\omega)} \ ,\end{aligned} \tag{3}$$

where β, γ and δ' are parameters depending on the material. Due to the homogeneity of the material, we also have $\nabla \cdot \mathbf{E}^{(\omega)} = 0$, therefore the first term in (3) vanishes. Moreover, following Ref. 16, we neglect the third term in (3). For these reasons we shall consider the following expression for the bulk SH source term:

$$\mathbf{P}_b^{(2\omega)} \cong \varepsilon_0 \, \gamma \nabla \left(\mathbf{E}^{(\omega)} \cdot \mathbf{E}^{(\omega)} \right) \ . \tag{4}$$

The surface nonlinear polarization contribution $\mathbf{P}_s^{(2\omega)}$ is given by:

$$\mathbf{P}_s^{(2\omega)} = \varepsilon_0 \, \overleftrightarrow{\chi}_s^{(2\omega)} \colon \mathbf{E}^{(\omega)} \mathbf{E}^{(\omega)} \text{ on } \Sigma \ , \tag{5}$$

where $\overleftrightarrow{\chi}_s^{(2\omega)}$ is the second-order surface nonlinear susceptibility. Since the nanoparticle surface has an isotropic symmetry with a mirror plane perpendicular to it, the surface susceptibility tensor $\overleftrightarrow{\chi}_s^{(2\omega)}$ has only three non-vanishing and independent elements, $\chi_{\perp\perp\perp}$, $\chi_{\perp\|\|}$ and $\chi_{\|\perp\|} = \chi_{\|\|\perp}$, where $\perp$ and $\|$ refer to the orthogonal and tangential components to the nanoparticle surface (Fig. 1(a)). Following Ref. 17, we neglect the component $\chi_{\perp\|\|}$, therefore:

$$\begin{aligned} \mathbf{P}_s^{(2\omega)} \cong \varepsilon_0 \, [& \chi_{\perp\perp\perp} \hat{\mathbf{n}}\hat{\mathbf{n}}\hat{\mathbf{n}} + \\ & \chi_{\|\perp\|} \left(\hat{\mathbf{t}}_1 \hat{\mathbf{n}} \hat{\mathbf{t}}_1 + \hat{\mathbf{t}}_2 \hat{\mathbf{n}} \hat{\mathbf{t}}_2 \right)] \colon \mathbf{E}^{(\omega)} \mathbf{E}^{(\omega)} \ . \end{aligned} \tag{6}$$

In order to calculate the SH radiation generated by the metallic sphere, we have to evaluate:

1. the electric field $\mathbf{E}^{(\omega)}$ in $\dot{\Omega}_i$ and on Σ, induced by the pump electromagnetic field $\left(\mathbf{E}_0^{(\omega)}, \mathbf{H}_0^{(\omega)} \right)$;
2. the bulk and surface SH sources generated by $\mathbf{E}^{(\omega)}$;
3. the SH electromagnetic fields $\left(\mathbf{E}^{(2\omega)}, \mathbf{H}^{(2\omega)} \right)$ radiated by the bulk and surface nonlinear polarization fields.

Both problems 1) and 3) are solved by expressing the unknown fields in terms of spherical vector wave functions (SVWFs), defined in Section II B. In Section III, we will study the SH generation from gold nano-spheres, using as values for $\chi_{\perp\perp\perp}$, $\chi_{\|\perp\|}$ and γ the expression in terms of the *Rudnick-Stern (R-S) parameters* (a, b, d), as done by Bachelier *et al.*:[17–19]

$$\chi_{\perp\perp\perp} = -\frac{a}{4} \chi_b(\omega) \frac{\omega_p^2}{\omega^2} \frac{\varepsilon_0}{e n_0}, \tag{7a}$$

$$\chi_{\|\perp\|} = -\frac{b}{2} \chi_b(\omega) \frac{\omega_p^2}{\omega^2} \frac{\varepsilon_0}{e n_0}, \tag{7b}$$

$$\gamma = -\frac{d}{8} \chi_b(\omega) \frac{\omega_p^2}{\omega^2} \frac{\varepsilon_0}{e n_0}, \tag{7c}$$

where $\chi_b = (\varepsilon_i/\varepsilon_0 - 1)$ is the bulk linear susceptibility of the metal, e is the electron charge (absolute value), n_0 is the number density of the conduction electrons and ω_p is the plasma frequency. By choosing $(a = 1, b = -1, d = 1)$, we obtain the *Rudnick-Stern* hydrodynamic model.[18] By measuring the SH generated by gold spherical nanoparticles with $R = 150nm$ at $\lambda = 800nm$, Bachelier et al. have found that an optimal choice for the phenomenological parameters a, b and d should be $(a = 0.5 - i0.25,\ b = 0.1,\ d = 1)$.[17]

The order of magnitude of the bulk SH polarization is thus given by:

$$P_b^{(2\omega)} = \epsilon_0 \left[\left(\frac{\lambda}{\lambda_p} \right)^2 \frac{E_0}{E_b} \right] \chi_b(\omega) E_0 \ , \tag{8}$$

where $\lambda_p = c_0 (2\pi/\omega_p)$ and $E_b = (\lambda_p/2\pi) e n_0/\varepsilon_0$. For noble metal nanoparticles $\lambda_p \cong 140\,nm$ and $E_b \approx 10^{14}\mathrm{V/m}$. The order of magnitude of the surface SH source is instead given by $P_s^{(2\omega)} = P_b^{(2\omega)} (\lambda_p/2\pi)$.

It is worth noting that the proposed analytical solution of the SH generation from a sphere is independent of the expression of $\chi_{\perp\perp\perp}$, $\chi_{\|\perp\|}$ and γ.

B. Electromagnetic fields at pump frequency

The electromagnetic field at the fundamental frequency is the solution of the Maxwell's equations:

$$\begin{cases} \nabla \times \mathbf{E}_i^{(\omega)} = -i\omega\mu_i \mathbf{H}_i^{(\omega)} \\ \nabla \times \mathbf{H}_i^{(\omega)} = +i\omega\varepsilon_i(\omega) \mathbf{E}_i^{(\omega)} \end{cases} \text{in } \Omega_i \ , \tag{9a}$$

$$\begin{cases} \mathbf{n} \times \left(\mathbf{H}_i^{(\omega)} - \mathbf{H}_{sc}^{(\omega)} \right) = \mathbf{n} \times \mathbf{H}_0^{(\omega)} \\ \mathbf{n} \times \left(\mathbf{E}_i^{(\omega)} - \mathbf{E}_{sc}^{(\omega)} \right) = \mathbf{n} \times \mathbf{E}_0^{(\omega)} \end{cases} \text{on } \Sigma \ , \tag{9b}$$

$$\begin{cases} \nabla \times \mathbf{E}_{sc}^{(\omega)} = -i\omega\mu_e \mathbf{H}_{sc}^{(\omega)} \\ \nabla \times \mathbf{H}_{sc}^{(\omega)} = +i\omega\varepsilon_e \mathbf{E}_{sc}^{(\omega)} \end{cases} \text{in } \Omega_e \ , \tag{9c}$$

where $\left(\mathbf{E}_i^{(\omega)}, \mathbf{H}_i^{(\omega)} \right)$ denote the fields in $\dot{\Omega}_i$ and $\left(\mathbf{E}_{sc}^{(\omega)}, \mathbf{H}_{sc}^{(\omega)} \right)$ denote the scattered fields in $\dot{\Omega}_e$, namely $\mathbf{E}_{sc}^{(\omega)} = \mathbf{E}_e^{(\omega)} - \mathbf{E}_0^{(\omega)}$ and $\mathbf{H}_{sc}^{(\omega)} = \mathbf{H}_e^{(\omega)} - \mathbf{H}_0^{(\omega)}$. Equations (9) have to be solved with the radiation condition at infinity for the scattered fields. Due to the symmetry of the problem, the general solution of the source-free Maxwell equations are expressed in each homogeneous region through the SVWFs $\mathbf{M}_{mn}^{(J)}$ and $\mathbf{N}_{mn}^{(J)}$:[20,21]

$$\mathbf{M}_{mn}^{(J)}(kr, \theta, \phi) = z_n^{(J)}(kr) \, \mathbf{X}_{mn}(\theta, \phi) \, , \tag{10a}$$

$$\mathbf{N}_{mn}^{(J)}(kr, \theta, \phi) = \frac{1}{k} \nabla \times \mathbf{M}_{mn}^{(J)}, \tag{10b}$$

where $z_n^{(J)} = z_n^{(J)}(kr)$ is one of the four kinds of the spherical Bessel functions, namely, Bessel function of the first kind $j_n = j_n(kr)$, or Bessel function of the second kind $y_n = y_n(kr)$, or Bessel function of the third kind (spherical Hankel functions of the first and second kind), $h_n^{(1)} = h_n^{(1)}(kr)$ and $h_n^{(2)} = h_n^{(2)}(kr)$, which we denote, respectively, with the apices $J = 1, 2, 3, 4$; $\mathbf{X}_{mn} = \mathbf{X}_{mn}(\theta, \phi)$ is a spherical vector harmonic (Appendix A). Here, both the spherical vector functions and the vector spherical harmonics are indexed by the order m and the degree n.

The incident plane-wave $\left(\mathbf{E}_0^{(\omega)}, \mathbf{H}_0^{(\omega)}\right)$ is decomposed in Eq. (11a) through the regular SVWFs, non-singular in the center of the sphere ($J = 1$), where E_0 is the amplitude of $\mathbf{E}_0$, and the coefficients $\left\{p_{mn}^{(\omega)}, q_{mn}^{(\omega)}\right\}$ are given in Appendix B for a linearly polarized state along the $x-$axis. Also the unknown fields $\left(\mathbf{E}_i^{(\omega)}, \mathbf{H}_i^{(\omega)}\right)$ in Ω_i $(0 \leq r < R)$, are decomposed through the regular SVWFs in Eq. (11b), where $\zeta_i(\omega) = \sqrt{\mu_i/\varepsilon_i(\omega)}$, $k_i(\omega) = \omega\sqrt{\varepsilon_i(\omega)\mu_i}$. The unknown scattered fields $\left(\mathbf{E}_{sc}^{(\omega)}, \mathbf{H}_{sc}^{(\omega)}\right)$ in $\dot{\Omega}_e$ (for $R < r$) are instead decomposed in Eq. (11c) through the radiative SVWFs, satisfying the radiation condition at infinity ($J = 3$).

$$
\begin{aligned}
\mathbf{E}_0^{(\omega)}(r,\theta,\phi) &= -E_0\sum_{n=1}^{\infty}\sum_{m=-n}^{n}\left\{q_{mn}^{(\omega)}\mathbf{M}_{mn}^{(1)}\left[k_e(\omega)r,\theta,\phi\right] + p_{mn}^{(\omega)}\mathbf{N}_{mn}^{(1)}\left[k_e(\omega)r,\theta,\phi\right]\right\}\\
\mathbf{H}_0^{(\omega)}(r,\theta,\phi) &= \frac{E_0}{i\zeta_e}\sum_{n=1}^{\infty}\sum_{m=-n}^{n}\left\{p_{mn}^{(\omega)}\mathbf{M}_{mn}^{(1)}\left[k_e(\omega)r,\theta,\phi\right] + q_{mn}^{(\omega)}\mathbf{N}_{mn}^{(1)}\left[k_e(\omega)r,\theta,\phi\right]\right\},
\end{aligned}
\tag{11a}
$$

$$
\begin{aligned}
\mathbf{E}_i^{(\omega)}(r,\theta,\phi) &= -E_0\sum_{n=1}^{\infty}\sum_{m=-n}^{n}\left\{c_{mn}^{(\omega)}\mathbf{M}_{mn}^{(1)}\left[k_i(\omega)r,\theta,\phi\right] + d_{mn}^{(\omega)}\mathbf{N}_{mn}^{(1)}\left[k_i(\omega)r,\theta,\phi\right]\right\}\\
\mathbf{H}_i^{(\omega)}(r,\theta,\phi) &= \frac{E_0}{i\zeta_i(\omega)}\sum_{n=1}^{\infty}\sum_{m=-n}^{n}\left\{d_{mn}^{(\omega)}\mathbf{M}_{mn}^{(1)}\left[k_i(\omega)r,\theta,\phi\right] + c_{mn}^{(\omega)}\mathbf{N}_{mn}^{(1)}\left[k_i(\omega)r,\theta,\phi\right]\right\},
\end{aligned}
\tag{11b}
$$

$$
\begin{aligned}
\mathbf{E}_{sc}^{(\omega)}(r,\theta,\phi) &= E_0\sum_{n=1}^{\infty}\sum_{m=-n}^{n}\left\{b_{mn}^{(\omega)}\mathbf{M}_{mn}^{(3)}\left[k_e(\omega)r,\theta,\phi\right] + a_{mn}^{(\omega)}\mathbf{N}_{mn}^{(3)}\left[k_e(\omega)r,\theta,\phi\right]\right\}\\
\mathbf{H}_{sc}^{(\omega)}(r,\theta,\phi) &= -\frac{E_0}{i\zeta_e}\sum_{n=1}^{\infty}\sum_{m=-n}^{n}\left\{a_{mn}^{(\omega)}\mathbf{M}_{mn}^{(1)}\left[k_e(\omega)r,\theta,\phi\right] + b_{mn}^{(\omega)}\mathbf{N}_{mn}^{(1)}\left[k_e(\omega)r,\theta,\phi\right]\right\}.
\end{aligned}
\tag{11c}
$$

The decomposition (11c) of $\left(\mathbf{E}_{sc}^{(\omega)}, \mathbf{H}_{sc}^{(\omega)}\right)$ satisfy Eq. (9c), and the decomposition (11b) of $\left(\mathbf{E}_i^{(\omega)}, \mathbf{H}_i^{(\omega)}\right)$ satisfy Eq. (9a). The unknown coefficients $\left\{a_{mn}^{(\omega)}, b_{mn}^{(\omega)}\right\}$ and $\left\{c_{mn}^{(\omega)}, d_{mn}^{(\omega)}\right\}$ are determined by requiring that the decompositions (11b,11c) also satisfy the boundary conditions (9b). The analytical expressions of $\left\{a_{mn}^{(\omega)}, b_{mn}^{(\omega)}\right\}$ and $\left\{c_{mn}^{(\omega)}, d_{mn}^{(\omega)}\right\}$ as functions of $\{p_{mn}, q_{mn}\}$ are given in Appendix C.

C. Electromagnetic fields at second harmonic

The SH electromagnetic field satisfies the Maxwell's equations:

$$
\begin{cases}
\nabla\times\mathbf{E}_i^{(2\omega)} = -2i\omega\mu_i\mathbf{H}_i^{(2\omega)}\\
\nabla\times\mathbf{H}_i^{(2\omega)} = 2i\omega\varepsilon_i(2\omega)\mathbf{E}_i^{(2\omega)} + \mathbf{J}_b^{(2\omega)}
\end{cases}
\quad \text{in } \hat{\Omega}_i,
\tag{12a}
$$

$$
\begin{cases}
\hat{\mathbf{n}}\times\left(\mathbf{H}_i^{(2\omega)} - \mathbf{H}_e^{(2\omega)}\right) = -\mathbf{j}_{elet}^{(2\omega)}\\
\hat{\mathbf{n}}\times\left(\mathbf{E}_i^{(2\omega)} - \mathbf{E}_e^{(2\omega)}\right) = \mathbf{j}_{mag}^{(2\omega)}
\end{cases}
\quad \text{on } \Sigma\ ,
\tag{12b}
$$

$$
\begin{cases}
\nabla\times\mathbf{E}_e^{(2\omega)} = -2i\omega\mu_e\mathbf{H}_e^{(2\omega)}\\
\nabla\times\mathbf{H}_e^{(2\omega)} = 2i\omega\varepsilon_e\mathbf{E}_e^{(2\omega)}
\end{cases}
\quad \text{in } \hat{\Omega}_e\ ,
\tag{12c}
$$

where

$$
\mathbf{J}_b^{(2\omega)} = 2i\omega\mathbf{P}_b^{(2\omega)},
\tag{13a}
$$

$$
\mathbf{j}_{elet}^{(2\omega)} = -2i\omega\hat{\mathbf{n}}\times\left(\hat{\mathbf{n}}\times\mathbf{P}_s^{(2\omega)}\right),
\tag{13b}
$$

$$
\mathbf{j}_{mag}^{(2\omega)} = \frac{1}{\varepsilon'}\hat{\mathbf{n}}\times\nabla_s\left(\hat{\mathbf{n}}\cdot\mathbf{P}_s^{(2\omega)}\right),
\tag{13c}
$$

the operator ∇_s denotes the surface gradient, $\left(\mathbf{E}_i^{(2\omega)}, \mathbf{H}_i^{(2\omega)}\right)$ denote the SH fields in $\dot{\Omega}_i$, $\left(\mathbf{E}_e^{(2\omega)}, \mathbf{H}_e^{(2\omega)}\right)$ denote the SH fields in $\dot{\Omega}_i$ and ε' is the *selvedge region* (see Appendix D) permittivity,[19] which we assumed equal to ε_0. The sources of the SH radiation, therefore, are of three types. The volume current density field $\mathbf{J}_b^{(2\omega)}$ given by Eq. (13a), takes into account the contribution of the SH bulk nonlinear polarization. The surface electric current density $\mathbf{j}_{elet}^{(2\omega)}$ given by Eq. (13b), takes into account the contribution of the SH tangent surface nonlinear polarization. The surface magnetic current density $\mathbf{j}_{mag}^{(2\omega)}$ given by (13c), takes into account the contribution of the SH normal surface nonlinear polarization (see Appendix D). The systems of Eq. (12a) have to be solved with the radiation condition at infinity for $\left(\mathbf{E}_e^{(2\omega)}, \mathbf{H}_e^{(2\omega)}\right)$.

The SH field equations are formally the same of the fundamental field equations except for the bulk source term $\mathbf{J}_b^{(2\omega)}$ in the Maxwell-Ampere equation and the substitutions $\omega \to 2\omega$. Consequently, the problem is reduced to that already solved for the fundamental fields, by expressing the electric field inside the nanoparticle as:

$$\mathbf{E}_i^{(2\omega)} = \mathbf{E}_{hom}^{(2\omega)} + \mathbf{E}_{part}^{(2\omega \text{in } \Omega_m)} \ , \tag{14}$$

where

$$\mathbf{E}_{part}^{(2\omega)} = -\frac{\varepsilon_0}{\varepsilon_i\left(2\omega\right)} \gamma \nabla \left(\mathbf{E}^{(\omega)} \cdot \mathbf{E}^{(\omega)}\right) . \tag{15}$$

The fields $\left(\mathbf{E}_{hom}^{(2\omega)}, \mathbf{H}_i^{(2\omega)}\right)$ and $\left(\mathbf{E}_e^{(2\omega)}, \mathbf{H}_e^{(2\omega)}\right)$ are solutions of the homogeneous Maxwell equations at frequency 2ω and have to satisfy the boundary equations:

$$\begin{cases} \hat{\mathbf{r}} \times \left(\mathbf{H}_i^{(2\omega)} - \mathbf{H}_e^{(2\omega)}\right) = -\mathbf{j}_{elet}^{(2\omega)} \\ \hat{\mathbf{r}} \times \left(\mathbf{E}_{hom}^{(2\omega)} - \mathbf{E}_e^{(2\omega)}\right) = \mathbf{j}_{mag}^{(2\omega)} - \hat{\mathbf{r}} \times \mathbf{E}_{part}^{(2\omega)} \end{cases} \text{on } \Sigma \tag{16}$$

Therefore we impose:

$$\begin{aligned} \mathbf{E}_{hom}^{(2\omega)}\left(r,\theta,\phi\right) &= -E_c^{(2\omega)} \sum_{n=1}^{\infty} \sum_{m=-n}^{n} \left\{ c_{mn}^{(2\omega)} \mathbf{M}_{mn}^{(1)} \left[k_i\left(2\omega\right) r, \theta, \phi\right] + d_{mn}^{(2\omega)} \mathbf{N}_{mn}^{(1)} \left[k_i\left(2\omega\right) r, \theta, \phi\right] \right\} \\ \mathbf{H}_i^{(2\omega)}\left(r,\theta,\phi\right) &= \frac{E_c^{(2\omega)}}{i\zeta_i\left(2\omega\right)} \sum_{n=1}^{\infty} \sum_{m=-n}^{n} \left\{ d_{mn}^{(2\omega)} \mathbf{M}_{mn}^{(1)} \left[k_i\left(2\omega\right) r, \theta, \phi\right] + c_{mn}^{(2\omega)} \mathbf{N}_{mn}^{(1)} \left[k_i\left(2\omega\right) r, \theta, \phi\right] \right\} \end{aligned} \quad \text{for } r < R, \text{ and} \tag{17a}$$

$$\begin{aligned} \mathbf{E}_e^{(2\omega)}\left(r,\theta,\phi\right) &= E_c^{(2\omega)} \sum_{n=1}^{\infty} \sum_{m=-n}^{n} \left\{ b_{mn}^{(2\omega)} \mathbf{M}_{mn}^{(3)} \left[k_e\left(2\omega\right) r, \theta, \phi\right] + a_{mn}^{(2\omega)} \mathbf{N}_{mn}^{(3)} \left[k_e\left(2\omega\right) r, \theta, \phi\right] \right\} \\ \mathbf{H}_e^{(2\omega)}\left(r,\theta,\phi\right) &= -\frac{E_c^{(2\omega)}}{i\zeta_e} \sum_{n=1}^{\infty} \sum_{m=-n}^{n} \left\{ a_{mn}^{(2\omega)} \mathbf{M}_{mn}^{(1)} \left[k_e\left(2\omega\right) r, \theta, \phi\right] + b_{mn}^{(2\omega)} \mathbf{N}_{mn}^{(1)} \left[k_e\left(2\omega\right) r, \theta, \phi\right] \right\} \end{aligned} \quad \text{for } r > R, \tag{17b}$$

where
$$E_c^{(2\omega)} = \left(\frac{\lambda}{\lambda_p}\right) \frac{E_0}{E_b} \chi_b\left(\omega\right) E_0 \tag{18}$$

is a characteristic electric field expressing the order of magnitude of the SH electric field in the nanoparticle. Both the expressions of $\left(\mathbf{E}_{hom}^{(2\omega)}, \mathbf{H}_i^{(2\omega)}\right)$ and $\left(\mathbf{E}_e^{(2\omega)}, \mathbf{H}_e^{(2\omega)}\right)$ satisfy the homogeneous Maxwell equations at frequency 2ω. The unknown coefficients $\left\{a_{mn}^{(2\omega)}, b_{mn}^{(2\omega)}\right\}$ and $\left\{c_{mn}^{(2\omega)}, d_{mn}^{(2\omega)}\right\}$ are evaluated by imposing that the functions (17) satisfies the boundary equations (16). The contribution of the SH bulk source, therefore, is given by the term $-\hat{\mathbf{r}} \times \mathbf{E}_{part}^{(2\omega)}|_\Sigma$ in the system of Eq. (16), playing the same role as the surface magnetic current $\mathbf{j}_{mag}^{(2\omega)}$. In order to analytically evaluate the coefficients $\left\{a_{mn}^{(2\omega)}, b_{mn}^{(2\omega)}\right\}$ and $\left\{c_{mn}^{(2\omega)}, d_{mn}^{(2\omega)}\right\}$, the fields $\mathbf{j}_{elet}^{(2\omega)}\left(\theta,\phi\right)$ and $\mathbf{j}_{mag}^{(2\omega)}\left(\theta,\phi\right) - \hat{\mathbf{r}} \times \mathbf{E}_{part}^{(2\omega)}\left(r=R,\theta,\phi\right)$ are expanded in terms of SVWFs:

$$\begin{aligned} \mathbf{j}_{elet}^{(2\omega)}\left(\theta,\phi\right) &= -\frac{E_c^{(2\omega)}}{i\zeta_e} \sum_{n=1}^{\infty} \sum_{m=-n}^{n} \left[{v'}_{mn}^{(2\omega)} \mathbf{X}_{mn}\left(\theta,\phi\right) + {u'}_{mn}^{(2\omega)} \hat{\mathbf{r}} \times \mathbf{X}_{mn}\left(\theta,\phi\right) \right] , \\ \mathbf{j}_{mag}^{(2\omega)}\left(\theta,\phi\right) - \hat{\mathbf{r}} \times \mathbf{E}_{part}^{(2\omega)}\left(r=R,\theta,\phi\right) &= -E_c^{(2\omega)} \sum_{n=1}^{\infty} \sum_{m=-n}^{n} \left[{u''}_{mn}^{(2\omega)} \hat{\mathbf{r}} \times \left[\hat{\mathbf{r}} \times \mathbf{X}_{mn}\left(\theta,\phi\right)\right] \right] , \end{aligned} \tag{19}$$

where the coefficients $\left\{{v'}_{mn}^{(2\omega)}, {u'}_{mn}^{(2\omega)}\right\}$ and $\left\{{u''}_{mn}^{(2\omega)}\right\}$ are evaluated in Appendix E. The formulas of the coefficients $u_{mn}^{(2\omega)}$ and $v_{mn}^{(2\omega)}$ obtained in this way are given in Appendix F.

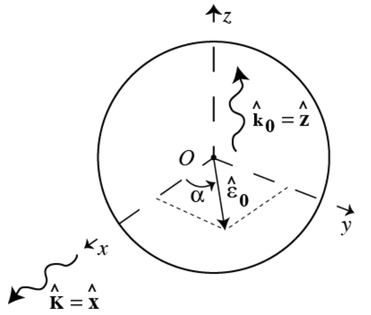
z
$\hat{\mathbf{k}}_0 = \hat{\mathbf{z}}$
O
α
$\hat{\varepsilon}_0$
y
x
$\hat{\mathbf{K}} = \hat{\mathbf{x}}$

FIG. 2. SH scattering geometry. The pump electromagnetic field propagates along the positive direction of the $z-$axis and is linearly polarized along $\hat{\varepsilon}_0$. The SH scattered field is observed along the direction $\hat{\mathbf{K}} = \hat{\mathbf{x}}$ (The scattering plane is xOz). The $y-$ and $z-$ components of the SH field are considered, respectively parallel ($\|$) and orthogonal ($\perp$) with respect to the scattering plane.

III. DISCUSSION: GOLD NANO-SPHERE

In the present section, by using the analytical solution derived in the previously, we analyze the SH generation from an isolated gold nano-sphere in vacuum, as the radius, the pump wavelength and polarization vary. Specifically, we study the SH radiation generated at pump wavelengths of $\lambda = 780$ nm (Ti:sapphire laser) and $\lambda = 520$ nm (gold plasmon resonance). Particular care has been devoted to the comparison with the existing theories in the Rayleigh regime. In order to model the bulk linear susceptibility of gold, we interpolated Johnson and Christy's experimental data.[22] We used two sets of values for the R-S parameters (see Eq. (7)) of the SH sources: the set ($a = 1,\ b = -1,\ d = 1$) proposed in Ref. 19 and the set ($a = 0.5 - i\,0.25,\ b = 0.1,\ d = 1$) proposed in Ref. 17.

The pump electromagnetic field is a plane-wave propagating along the positive direction of the $z-$axis, and linearly polarized in the xy plane, with a polarization direction $\hat{\boldsymbol{\varepsilon}}_0$. We indicate with α the angle between the unit vector $\hat{\boldsymbol{\varepsilon}}_0$ and $x-$axis (the reference versus is counterclockwise, seen from the semispace $z > 0$), as shown in Fig. 2.

We investigate the SH power per unit solid angle $\frac{dP^{(2\omega)}_{\hat{\varepsilon}^*}(\hat{\mathbf{K}})}{d\Omega}$, radiated in the farfield along the direction $\hat{\mathbf{K}}$ and collected by an analyzer with polarization state $\hat{\boldsymbol{\varepsilon}}^*$:

$$\frac{dP^{(2\omega)}_{\hat{\varepsilon}^*}\left(\hat{\mathbf{K}}\right)}{d\Omega} = \lim_{r\to\infty}\left[\frac{r^2}{2\zeta_e}\left|\hat{\varepsilon}^* \cdot \mathbf{E}^{(2\omega)}_e\left(\hat{\mathbf{K}}\right)\right|^2\right] , \qquad (20)$$

and the SH scattering cross-section $C^{(2\omega)}_{sca}$:

$$C^{(2\omega)}_{sca} = \lim_{\rho\to\infty}\frac{\int_{\Sigma_\rho}\left|\mathbf{E}^{(2\omega)}_e\right|^2 \cdot \hat{\mathbf{n}}\, d\Sigma}{\left|\mathbf{E}^{(\omega)}_0\right|^2}, \qquad (21)$$

where Σ_ρ is a spherical surface with radius ρ, centered at the origin of the coordinate system. $\frac{dP^{(2\omega)}_{\hat{\varepsilon}^*}(\hat{\mathbf{K}})}{d\Omega}$ depends on the collection direction $\hat{\mathbf{K}}$ of the scattered SH light. $C^{(2\omega)}_{sca}$ has the physical dimensions of an area, and is proportional to the SH generation efficiency. In order to analyze the SH radiation polarization state, the analyzer can be polarized either parallel ($\|$) or perpendicular ($\perp$) to the SH scattering plane, defined by the propagation direction $\hat{\boldsymbol{k}}_0$ of the pump wave, and the collection direction ($\hat{\mathbf{K}}$). We denote with $dP^{(2\omega)}_{\|}/d\Omega$ and $dP^{(2\omega)}_{\perp}/d\Omega$ the radiated powers per unit solid angle associated to the $\|$ and $\perp$ components. The analysis of the polarization state of SH radiation collected at right angle from the pump beam, *i.e.* $\hat{\boldsymbol{K}} = \hat{\boldsymbol{x}}$, is very important because it allows to discriminate the radiation generated by even and odd SH multipole sources. Indeed, only the SH $\mathbf{N}^{(3)}_{mn}$ multipoles with odd n contribute to the $\|$ component and only the SH $\mathbf{N}^{(3)}_{mn}$ multipoles with even n contribute to the $\perp$ component. This behavior is reversed for the SH $\mathbf{M}^{(3)}_{mn}$ multipoles.

A. SH source currents: Rayleigh and Mie regimes

Here we analyze the SH radiation generated from the single nonlinear sources, acting as if they were radiating independently. Fig. 3 shows the magnitude of each SH source current density, namely $\mathbf{J}^{(2\omega)}_b$, $\mathbf{j}^{(2\omega)}_{elet}$, $\mathbf{j}^{(2\omega)}_{mag}$, normalized to its own maximum, and computed for the two pump wavelengths $\lambda = 520$ nm and $\lambda = 780$ nm, corresponding to resonance and off-resonance conditions, respectively. Two nanoparticle radii have been considered, namely a particle with small size ($R = 10$ nm) and a particle comparable in size to the pump wavelength ($R = 150$ nm). The pump field is linearly polarized along the $x-$axis ($\alpha = 0$). In particular, the first column (panels a-d) shows the magnitude of the bulk electric current density $\mathbf{J}^{(2\omega)}_b$ in the xOz plane, while the second and third columns (panels e-h,i-l), show the magnitude of the surface electric $\mathbf{j}^{(2\omega)}_{elet}$ and magnetic $\mathbf{j}^{(2\omega)}_{mag}$ current densities, respectively. For small particles, $\mathbf{J}^{(2\omega)}_b$ is significant across the entire particle volume (panel a, b). In particular, while for $\lambda = 520$ nm (panel a) $\mathbf{J}^{(2\omega)}_b$ decreases along the direction of forward scattering, for $\lambda = 780$nm it is almost uniform. For particles with larger size (panels c,d), the skin effect appears, *i.e.* the current $\mathbf{J}^{(2\omega)}_b$ is strongly confined near the particle surface. The intensity distribution of both $\mathbf{j}^{(2\omega)}_{elet}$ and $\mathbf{j}^{(2\omega)}_{mag}$ (e,f,i,j) is symmetric around the polarization direction of the pump field for small particles. As the radius increases, this holds no longer true due to the onset of higher order multipoles (panels g,h,k,l). It is worth noting that the surface electric current density $\mathbf{j}^{(2\omega)}_{elet}$ vanishes on a circle lying in the yOz plane, for any particle size and pump wavelength, as shown in panels (e-h), due to the rotational symmetry of the particle. Similarly, the surface magnetic current

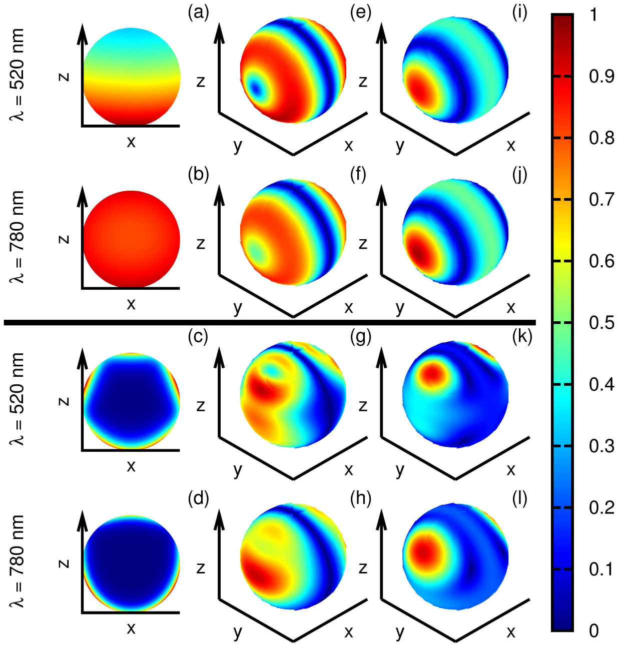

FIG. 3. SH source current distribution excited by a pump field linearly polarized along x. The nano-sphere size is $R = 10$ nm (first and second row)and $R = 150$ nm (third and fourth row), the pump wavelength is $\lambda = 520$ nm (first and third rows) and $\lambda = 780$ nm (second and fourth rows). Panels (a,b,c,d) are relative to the bulk current density cut in the xOz plane, panels (e,f,g,h) are relative to the surface electric current density and panels (i,j,k,l) are relative to the surface magnetic current density. Each panel shows the current magnitude normalized to its own maximum.

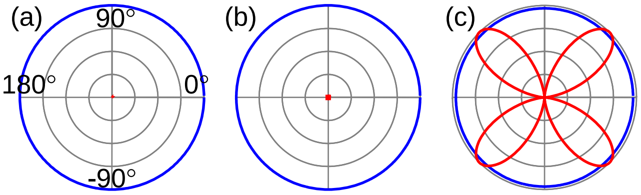

FIG. 4. SH power per unit solid angle collected at right angle from the pump beam (Fig. 2) as function of the pump polarization angle α, for a nano-sphere with $R = 10\,nm$. The pump wavelength is $780\,nm$. The blue line corresponds to the $\parallel$ component and the red line to the $\perp$ component with respect to the scattering plane. All the graphs are normalized to the maximum of the most intense component. Panel (a) is relative to the bulk current, panel (b) to the surface electric current, panel (c) to the the surface magnetic current, as if they acted separately.

density $\mathbf{j}_{mag}^{(2\omega)}$ displays a circle with a constant magnitude for every particle size, as shown in panels (i-l).

In Fig. 4 the SH power per unit solid angle collected at right angle from the pump direction is shown for a nano-sphere with $R = 10\,nm$. Panels (a), (b) and (c) are relevant to the SH radiation generated by the bulk, surface electric and surface magnetic SH source currents, respectively, as if they acted separately. The blue and red lines correspond respectively to $dP_{\parallel}^{(2\omega)}/d\Omega$ and $dP_{\perp}^{(2\omega)}/d\Omega$, and for each panel both the components are normalized to the maximum of the most intense.

These results agree with those obtained analyzing the SH radiation from a metal nano-sphere in the Rayleigh limit.[9,13] In this regime, the SH radiation coincides with the electromagnetic field radiated by a fictitious electric dipole with effective moment $\mathbf{p}_{eff}^{(2\omega)}(\hat{\mathbf{r}}) \cong \mathbf{p}^{(2\omega)} + i\,k_0 \overleftrightarrow{\mathbf{Q}}^{(2\omega)}\hat{\mathbf{r}}/3$, where $\mathbf{p}^{(2\omega)}$ is the induced SH electric dipole moment ($n = 1$) and $\overleftrightarrow{\mathbf{Q}}^{(2\omega)}$ is the induced SH electric quadrupole moment ($n = 2$). Depending on the component of the SH intensity, two different shapes of the polarization diagrams arise. For each SH source, $dP_{\parallel}^{(2\omega)}/d\Omega$ is due to a SH dipolar electric mode aligned along the propagation direction of the pump,[9,13] therefore its value is independent of the polarization angle of the pump. On the other hand, the four lobe pattern observed for $dP_{\perp}^{(2\omega)}/d\Omega$ is due to a SH quadrupolar mode. Furthermore, $dP_{\perp}^{(2\omega)}/d\Omega$ is negligible for both $\mathbf{J}_b^{(2\omega)}$ and $\mathbf{j}_{elet}^{(2\omega)}$, while it is comparable with $dP_{\parallel}^{(2\omega)}/d\Omega$ for $\mathbf{j}_{mag}^{(2\omega)}$. For larger particles, higher order SH multipoles arise due to larger retardation effects, significantly modifying the SH radiation characteristics, as we shall see in the next section.

B. SH scattering cross-section

In this Section, we study the SH scattering cross-section $C_{sca}^{(2\omega)}$ for a gold nano-sphere, using as R-S parameters the values ($a = 1, b = -1, d = 1$). All the results are relative to the case of a pump plane-wave with electric field of unitary magnitude, *i.e.* $|E_0| = 1\;Vm^{-1}$. Figure 5 shows $C_{sca}^{(2\omega)}$ as function of the pump wavelength (black lines), for four particle sizes. For all the investigated sizes, $C_{sca}^{(2\omega)}$ shows a maximum at $\lambda \approx 520\,nm$, when the pump wavelength matches the plasmonic resonance of the particle. Another local maximum is also observed at $\lambda \approx 1040\,nm$. At this wavelength the SH fields resonate in the gold nano-sphere. The relative intensity of $C_{sca}^{(2\omega)}$ at $\lambda \approx 1040\,nm$ increases as the particle size increases. A third local maximum can be observed at $\lambda \approx 700\,nm$, for certain particle sizes (*e.g.* $R = 100\,nm$ and $R = 200\,nm$). Similar trends, not shown here, have been found with the set of values ($a = 0.5 - i0.25, b = 0.1, d = 1$) for the R-S parameters.

In order to unveil the origin of the SH radiation in the Rudnick-Stern model, the contributions of each multipole are shown, up to the $6th$ order. For $R = 10\,nm$ (panel a), $C_{sca}^{(2\omega)}$ is mostly due to the SH dipolar source, and only for short wavelengths the SH quadrupolar source begins to be significant. As we increase the radius R to 100 nm (panel b), we can identify three different regimes: for short wavelengths $\lambda < 550\,nm$, $C_{sca}^{(2\omega)}$ is dominated

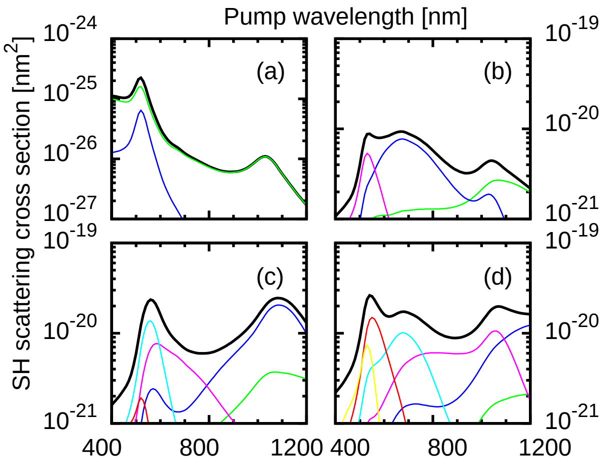

FIG. 5. SH scattering cross-section (black line) as function of the pump wavelength for nano-spheres with $R = 10\,nm$ (a), $R = 100\,nm$ (b), $R = 150\,nm$ (c), $R = 200\,nm$ (d), with $(a = 1, b = -1, d = 1)$. The contribution of each multipolar order to the total radiation cross-section is shown up to the 6th: $n = 1$ (green), $n = 2$ (blue), $n = 3$ (violet), $n = 4$ (cyan), $n = 5$ (red), $n = 6$ (yellow).

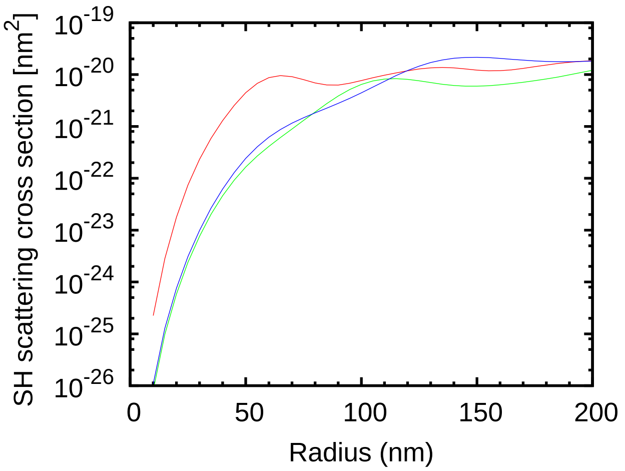

FIG. 6. SH scattering cross-section as function of the nano-sphere radius R at pump wavelengths $\lambda = 520\,nm$ (red), $\lambda = 780\,nm$ (green), $\lambda = 1040\,nm$ (blue), obtained with $(a = 1, b = -1, d = 1)$.

by the octupolar source, the quadrupolar one prevails in the range $550\,nm < \lambda < 950\,nm$, while the dipolar source is the most intense for large wavelengths. For a particle with $R = 150\,nm$ (panel c), the dipolar source is negligible regardless of the pump wavelength, and the main contributions to $C_{sca}^{(2\omega)}$ arise from the multipoles with $n = 2, 3, 4$. Similarly, the main contributions for a particle with $R = 200\,nm$ arise from $n = 2, 3, 4$ for large wavelength, and from the multipoles $n = 5, 6$ for short wavelengths.

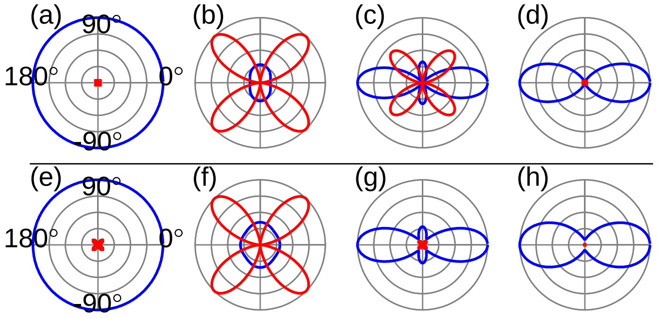

FIG. 7. SH power per unit solid angle collected at right angle from the pump beam (Fig. 2) as function of the pump polarization angle α, for nano-sphere with $R = 10\,nm$ (a,e), $R = 100\,nm$ (b,f), $R = 150\,nm$ (c,g), $R = 200\,nm$ (d,h), obtained by using (a-d) $(a = 1, b = -1, d = 1)$ and (e-h) $(a = 0.5 - i0.25, b = 0.1, d = 1)$. The pump wavelength is $\lambda = 780nm$. The blue line corresponds to the $\parallel$ component and the red line to the $\perp$ component with respect to the scattering plane. All the graphs are normalized to the maximum of the most intense component.

Figure 6 shows the SH scattering cross-section as function of the nanoparticle radius, for three values of the pump wavelength ($\lambda = 520\,nm$, $780\,nm$, $1040\,nm$). The SH scattering cross-section increases more than 4 orders of magnitude when the particle size increases up to $R = 100\,nm$. For larger radii, the SH scattering cross-section saturates and a small modulation takes place. For small particle size, the highest cross-section is shown when the particle is in plasmonic resonance (i.e., red curve). For larger particle size, the magnitude of $C_{sca}^{(2\omega)}$ is comparable for all the investigated pump wavelengths. Also in this case, similar trends have been found using the set of R-S parameters $(a = 0.5 - i0.25, b = 0.1, d = 1)$.

C. SH power dependence on the pump polarization

The SH power radiated at right angle from the propagation direction of the pump allows for the recognition of even- and odd-order multipolar contributions to the SH generation process, as already pointed out. Figure 7 shows $dP_{\parallel}^{(2\omega)}/d\Omega$ and $dP_{\perp}^{(2\omega)}/d\Omega$ as function of the polarization angle α of the pump, for two different choices of R-S parameters. The first row (a-d) is relative to the R-S parameter set $(a = 1, b = -1, d = 1)$, while the second row (e-h) is relative to the set $(a = 0.5 - i0.25, b = 0.1, d = 1)$. Four different values of particle size are presented: $R = 10\,nm$ (a,e), $R = 100\,nm$ (b,f), $R = 150\,nm$ (c,g), $R = 200\,nm$ (d,h). Both of $dP_{\parallel}^{(2\omega)}/d\Omega$ and $dP_{\perp}^{(2\omega)}/d\Omega$ are normalized to the maximum of the most intense component. For small (a,e) and very large (d,h) radii, $dP_{\parallel}^{(2\omega)}/d\Omega$ prevails over the $dP_{\perp}^{(2\omega)}/d\Omega$ for both sets of the R-S parameters. For intermediate sizes (b,c,f,g), $dP_{\parallel}^{(2\omega)}/d\Omega$ and $dP_{\perp}^{(2\omega)}/d\Omega$ are comparable, and their relative intensities strongly depend

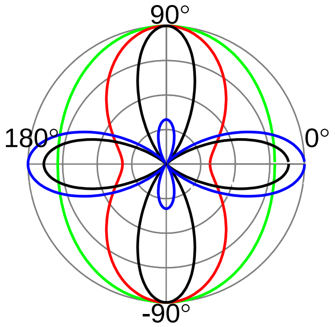

FIG. 8. SH power per unit solid angle of the $\parallel$ component collected at right angle from the pump beam (Fig. 2), as function of the pump polarization angle α, for nano-spheres of size $R = 80\,nm$ (green), $R = 120\,nm$ (red), $R = 140\,nm$ (black), $R = 150\,nm$(blue) and $(a = 1, b = -1, d = 1)$. The pump wavelength is $\lambda = 780 nm$, all the curves are normalized to their own maximum.

on the particular choice of the R-S parameters. For small particles, $dP_{\parallel}^{(2\omega)}/d\Omega$ is independent of the polarization angle α (panels a,e), while up to 4 lobes can appear for larger particles, as it will be shown more in detail in Fig. 8. The graphs of the component $dP_{\perp}^{(2\omega)}/d\Omega$ feature four lobes oriented along the bisectors of the 4 quadrants, in each of the investigated case.

The appearance of an octupolar SH source significantly modifies the shape of $dP_{\parallel}^{(2\omega)}/d\Omega$. In the Rayleigh limit the $\parallel$ component generated by the SH dipolar source fully prevails over the $\perp$ component generated by the SH quadrupolar source. As the radius increases, the intensity of the SH octupolar source increases due to the retardation effects, as pointed out in the previous section. Due to the interference in the far field of the SH dipolar and octupolar fields, the $dP_{\parallel}^{(2\omega)}/d\Omega$ reduces significantly until it becomes smaller than $dP_{\perp}^{(2\omega)}/d\Omega$ (b,c). As the radius further increases, the SH octupolar source prevails over the SH dipolar source, and the shape of $dP_{\parallel}^{(2\omega)}/d\Omega$ gets close to that of an octupole (d,e).

The details of the transition from the dipole to the octupole pattern as the radius increases are shown in Fig. 8. First, the circular shape of $dP_{\parallel}^{(2\omega)}/d\Omega$ is shrunk along the directions $\alpha = 0°, 180°$, until the amplitude reaches a null (green and red curves). Then, two lobes arise along these directions (black curve), forming a four-lobe pattern. As the radius further increases, the intensities of the two lobes along the directions at $\alpha = 0°, 180°$ prevail over the intensities of the lobes along the directions at $\alpha = 90°, 270°$ (blue curve). In conclusion, even some discrepancies arise from the comparison between the results obtained by using the two sets of R-S parameters, the main features of the SH radiation field are common.

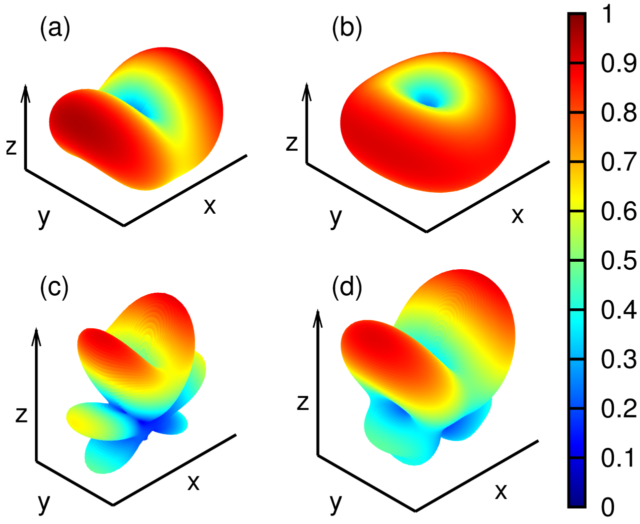

FIG. 9. SH radiation diagrams for nano-spheres of size $R = 10\,nm$ (panels a,b), $R = 150\,nm$ (panel c, d), obtained by using $(a = 1, b = -1, d = 1)$. Panels (a, c) are relative to the pump wavelength $\lambda = 520\,nm$, and panels (b,d) to $\lambda = 780\,nm$. All the intensities are normalized to their own maximum.

D. SH radiation diagrams

Figure 9 shows the angular distribution of the SH radiation generated by gold nano-spheres, obtained using the R-S parameters $(a = 1,\ b = -1,\ d = 1)$. The first row (a,b) is relative to a small sphere $(R = 10\,nm)$ and the second row (c,d) to a large sphere $(R = 150\,nm)$. In the first column (a,c) the pump wavelength is $\lambda = 520\,nm$, while in the second column (b,d) $\lambda = 780\,nm$.

For particles with $R = 10\,nm$, the dipolar and quadrupolar SH sources dominates the response, in agreement with the Rayleigh limit. In particular, we notice that the quadrupolar SH source is more important at $\lambda = 520\,nm$, while at $\lambda = 780\,nm$ the dipolar mode fully dominates the response. As the particle radius increases, higher order modes come into play, resulting in an higher number of secondary lobes. For particles with $R = 150\,nm$, the octupolar mode dominates the angular distribution of the SH radiation at $\lambda = 780\,nm$. Moreover, for each particle size and pump wavelength, the lobes display a preferential alignment along the polarization direction of the pump field.

Figure 10 shows the two cuts of the 3D radiation diagram along the xOz, and yOz plane. It is worth noting that the SH power vanishes in both the forward- and backward-scattering directions, regardless of R. This selection rule is a direct consequence of the rotational symmetry of the sphere around the propagation direction of the pump. Two lobes, directed orthogonally to the pump propagation direction, characterize the radiation diagrams of small particles. As the particle size increases, the lobes with higher power tend to come closer to the forward direction, while the lobes in the backward direc-

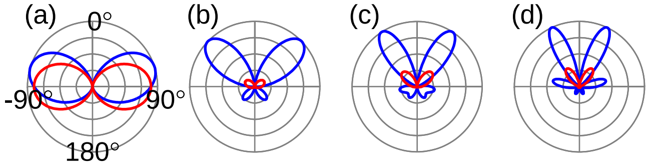

FIG. 10. SH radiation diagrams as function of θ angle, at $\varphi = 0°$ (blue) and $\varphi = 90°$ (red), for nano-spheres of size $R = 10\,nm$ (a), $R = 100\,nm$ (b), $R = 150\,nm$ (c), and $R = 200\,nm$ (d) and $(a = 1, b = -1, d = 1)$. The pump wavelength is $\lambda = 780\,nm$, for each panel the curves are normalized to the maximum of the most intense one.

tion decrease in amplitude. The same trend is observed if the particle size is fixed and the pump wavelength decreases. This behavior has been already observed experimentally for silver nanoparticles in Ref. 23.

IV. CONCLUSIONS

We have developed a full-wave analytical solution for the second-harmonic generation from a spherical particle of arbitrary size, made of lossy centrosymmetric material. This approach extends the existing theories, enabling a rigorous treatment of all the sources of SH radiation, located both on the surface and in the bulk of the particle. The solution of the problem is derived in the framework of the Mie theory by expanding the pump field, the nonlinear polarization sources and the second harmonic fields in series of spherical vector wave functions, and enforcing the boundary conditions at the sphere surface.

Using the developed method, we investigated the spatial distribution of bulk and superficial non-linear sources. We also studied the SH radiated power as function of the pump polarization angle, the SH radiation cross section spectrum and the radiation diagrams.

The application of the proposed method in combination with experimental observation, can improve the general understanding of nonlinear processes in metals, and can lead to an accurate evaluation of weights for the different SH sources. The theory of SH scattering can be easily extended to the multiparticle case. This approach can also guide the design of novel nanoplasmonic devices with enhanced SHG emission for a wide range of applications,[24] including sensors for probing physical and chemical properties of material surfaces.

Appendix A: Vector spherical harmonics

The vector spherical harmonics $\mathbf{X}_{mn}$ are:[20,21]

$$\mathbf{X}_{mn}(\theta,\phi) = i\frac{1}{\sqrt{n(n+1)}}\sqrt{\frac{2n+1}{4\pi}\frac{(n-m)!}{(n+m)!}}\cdot \left[i\pi_{mn}(\cos\theta)\,\hat{\theta} - \tau_{mn}(\cos\theta)\,\hat{\phi}\right]e^{im\phi}\ ,$$

$$\text{where}\quad \begin{aligned}\pi_{mn}(\cos\theta) &= \frac{m}{\sin\theta}P_n^m(\cos\theta)\\ \tau_{mn}(\cos\theta) &= \frac{d}{d\theta}P_n^m(\cos\theta)\end{aligned}\ ,$$

and $P_n^m = P_n^m(u)$ is the associated Legendre function of the first kind and of degree n and m.

Appendix B: Calculation of $\left\{p_{mn}^{(\omega)}, q_{mn}^{(\omega)}\right\}$

The expansion coefficients in Eq. (11a), for a linearly polarized plane-wave propagating along the $z-$axis with the electric field parallel to the $x-$axis (Fig. 1a), are:

$$p_{mn}^{(\omega)} = q_{mn}^{(\omega)} = 0, \text{ for } |m| \neq 1$$
$$p_{1n}^{(\omega)} = q_{1n}^{(\omega)} = -p_{-1n}^{(\omega)} = q_{-1n}^{(\omega)} = \frac{1}{2}(-i)^n\sqrt{4\pi(2n+1)}$$

Appendix C: Calculation of $\left\{a_{mn}^{(\omega)}, b_{mn}^{(\omega)}\right\}$, $\left\{c_{mn}^{(\omega)}, d_{mn}^{(\omega)}\right\}$

The coefficients $\left\{a_{mn}^{(\omega)}, b_{mn}^{(\omega)}\right\}$ and $\left\{c_{mn}^{(\omega)}, d_{mn}^{(\omega)}\right\}$ are expressed as

$$\frac{a_{mn}^{(\omega)}}{p_{mn}^{(\omega)}} = \frac{\frac{\zeta_e}{\zeta_i(\omega)}\,\psi_n(x_i^{(\omega)})\,\dot{\psi}_n(x_e^{(\omega)}) - \psi_n(x_e^{(\omega)})\,\dot{\psi}_n(x_i^{(\omega)})}{\frac{\zeta_e}{\zeta_i(\omega)}\,\psi_n(x_i^{(\omega)})\,\dot{\xi}_n(x_e^{(\omega)}) - \xi_n(x_e^{(\omega)})\,\dot{\psi}_n(x_i^{(\omega)})}$$
$$\frac{b_{mn}^{(\omega)}}{q_{mn}^{(\omega)}} = \frac{\psi_n(x_i^{(\omega)})\,\dot{\psi}_n(x_e^{(\omega)}) - \frac{\zeta_e}{\zeta_i(\omega)}\,\psi_n(x_e^{(\omega)})\,\dot{\psi}_n(x_i^{(\omega)})}{\psi_n(x_i^{(\omega)})\,\dot{\xi}_n(x_e^{(\omega)}) - \frac{\zeta_e}{\zeta_i(\omega)}\,\xi_n(x_e^{(\omega)})\,\dot{\psi}_n(x_i^{(\omega)})}$$
$$\frac{c_{mn}^{(\omega)}}{q_{mn}^{(\omega)}} = \frac{i\frac{k_i(\omega)}{k_e(\omega)}}{\psi_n(x_i^{(\omega)})\,\dot{\xi}_n(x_e^{(\omega)}) - \frac{\zeta_e}{\zeta_i(\omega)}\,\xi_n(x_e^{(\omega)})\,\dot{\psi}_n(x_i^{(\omega)})}$$
$$\frac{d_{mn}^{(\omega)}}{p_{mn}^{(\omega)}} = \frac{i\frac{k_i(\omega)}{k_e(\omega)}}{\frac{\zeta_e}{\zeta_i(\omega)}\,\psi_n(x_i^{(\omega)})\,\dot{\xi}_n(x_e^{(\omega)}) - \xi_n(x_e^{(\omega)})\,\dot{\psi}_n(x_i^{(\omega)})}$$

where $x_e^{(\omega)} = k_e^{(\omega)}R$, $x_i^{(\omega)} = k_i^{(\omega)}$ and $\psi_n = \psi_n(\rho)$, $\xi_n = \xi_n(\rho)$ are the Riccati-Bessel functions defined as $\psi_n(\rho) = \rho\ j_n(\rho)$, $\xi_n = \rho\ h_n^{(1)}(\rho)$. $\dot{\zeta}$ denotes the first derivative of $\zeta = \zeta(\rho)$ with respect to ρ.

Appendix D: Selvedge region

The selvedge region (Fig. 1b) is a layer of infinitesimal depth δ at the interface metal-vacuum. In this region there is a volumetric current density $\mathbf{J}_{s\perp}^{(2\omega)} = i2\omega\left(\mathbf{P}_s^{(2\omega)}\cdot\mathbf{n}/\delta\right)\mathbf{n}$, which is exactly compensated by the normal component of the displacement current density, $\mathbf{J}_{s\perp}^{(2\omega)} + i2\omega\mathbf{D}_{\perp}^{(2\omega)} = \mathbf{0}$, otherwise there would be an unbounded magnetic field. Therefore, in the selvedge region, $\mathbf{D}_{\perp}^{(2\omega)} = -\left(\mathbf{P}_s^{(2\omega)}\cdot\mathbf{n}/\delta\right)\mathbf{n}$. From the

Faraday-Neumann's law, applied to the elementary curve Δl shown in Figure 1b, we have $\left(\mathbf{E}_i^{(2\omega)} - \mathbf{E}_e^{(2\omega)}\right)|_\Sigma \cdot \Delta l_\parallel = u_2 - u_1$, where $u_{(\alpha)} = \int_{\Delta l_\perp^{(\alpha)}} \mathbf{E}^{(2\omega)} \cdot d\boldsymbol{l} = \left(\mathbf{P}_s^{(2\omega)} \cdot \hat{\mathbf{n}}\right)\Big|_{Q^{(\alpha)}}$ and $\alpha = 1, 2$. By combining these relations we obtain the equations $\hat{\mathbf{n}} \times \left(\mathbf{E}_i^{(2\omega)} - \mathbf{E}_e^{(2\omega)}\right)\Big|_\Sigma = \hat{\mathbf{n}} \times \nabla_S \left(\mathbf{P}_s^{(2\omega)} \cdot \hat{\mathbf{n}}\right)/\varepsilon'$.

Appendix E: Calculation of $\left\{a_{mn}^{(2\omega)}, b_{mn}^{(2\omega)}\right\}$, $\left\{c_{mn}^{(2\omega)}, d_{mn}^{(2\omega)}\right\}$

The coefficients $\left\{a_{mn}^{(2\omega)}, b_{mn}^{(2\omega)}\right\}$ and $\left\{c_{mn}^{(2\omega)}, d_{mn}^{(2\omega)}\right\}$ are expressed as:

$$\begin{aligned} a_{mn}^{(2\omega)} &= a'^{(2\omega)}_{mn} + a''^{(2\omega)}_{mn}\ , \quad & b_{mn}^{(2\omega)} &= b'^{(2\omega)}_{mn} + b''^{(2\omega)}_{mn}\ , \\ c_{mn}^{(2\omega)} &= c'^{(2\omega)}_{mn} + c''^{(2\omega)}_{mn}\ , \quad & d_{mn}^{(2\omega)} &= d'^{(2\omega)}_{mn} + d''^{(2\omega)}_{mn}\ , \end{aligned}$$

where with one apex we denote the contribution due to the tangential surface SH sources and with two apices we denote the contributions of both the normal surface SH sources and the bulk SH sources. For the contribution of the tangential surface SH sources we have:

$$\frac{a'^{(2\omega)}_{mn}}{u'^{(2\omega)}_{mn}} = \frac{x_e^{(2\omega)} \dot{\psi}_n(x_i^{(2\omega)})}{\xi_n(x_e^{(2\omega)})\dot{\psi}_n(x_i^{(2\omega)}) - \frac{\zeta_e}{\zeta_i(2\omega)}\psi_n(x_i^{(2\omega)})\dot{\xi}_n(x_e^{(2\omega)})}$$

$$\frac{b'^{(2\omega)}_{mn}}{v'^{(2\omega)}_{mn}} = \frac{x_e^{(2\omega)} \psi_n(x_i^{(2\omega)})}{\frac{\zeta_e}{\zeta_i(2\omega)}\xi_n(x_e^{(2\omega)})\dot{\psi}_n(x_i^{(2\omega)}) - \psi_n(x_i^{(2\omega)})\dot{\xi}_n(x_e^{(2\omega)})}$$

$$\frac{c'^{(2\omega)}_{mn}}{v'^{(2\omega)}_{mn}} = \frac{x_i^{(2\omega)} \xi_n(x_e^{(2\omega)})}{\psi_n(x_i^{(2\omega)})\dot{\xi}_n(x_e^{(2\omega)}) - \frac{\zeta_e}{\zeta_i(2\omega)}\xi_n(x_e^{(2\omega)})\dot{\psi}_n(x_i^{(2\omega)})}$$

$$\frac{d'^{(2\omega)}_{mn}}{u'^{(2\omega)}_{mn}} = \frac{x_i^{(2\omega)} \dot{\xi}_n(x_e^{(2\omega)})}{\frac{\zeta_e}{\zeta_i(2\omega)}\psi_n(x_i^{(2\omega)})\dot{\xi}_n(x_e^{(2\omega)}) - \xi_n(x_e^{(2\omega)})\dot{\psi}_n(x_i^{(2\omega)})}$$

where the coefficients $\left\{u'^{(2\omega)}_{mn}, v'^{(2\omega)}_{mn}\right\}$ are given in Appendix F, $x_e^{(2\omega)} = k_e^{(2\omega)}R$, $x_i^{(2\omega)} = k_i^{(2\omega)}R$, $\psi_n = \psi_n(\rho)$, $\xi_n = \xi_n(\rho)$ are the Riccati-Bessel functions.

For the contribution of both the normal surface SH sources and the bulk SH sources we have:

$$\frac{a''^{(2\omega)}_{mn}}{u''^{(2\omega)}_{mn}} = \frac{\frac{\zeta_e}{\zeta_i(2\omega)} x_e^{(2\omega)} \psi_n(x_i^{(2\omega)})}{\frac{\zeta_e}{\zeta_i(2\omega)}\psi_n(x_i^{(2\omega)})\dot{\xi}_n(x_e^{(2\omega)}) - \xi_n(x_e^{(2\omega)})\dot{\psi}_n(x_i^{(2\omega)})}$$

$$b''^{(2\omega)}_{mn} = 0$$

$$c''^{(2\omega)}_{mn} = 0$$

$$\frac{d''^{(2\omega)}_{mn}}{u''^{(2\omega)}_{mn}} = \frac{x_i^{(2\omega)} \xi_n(x_e^{(2\omega)})}{\xi_n(x_e^{(2\omega)})\dot{\psi}_n(x_i^{(2\omega)}) - \frac{\zeta_e}{\zeta_i(2\omega)}\psi_n(x_i^{(2\omega)})\dot{\xi}_n(x_e^{(2\omega)})}$$

where the coefficients $\left\{u''^{(2\omega)}_{mn}, v''^{(2\omega)}_{mn}\right\}$ are given in Appendix F.

Appendix F: Calculation of $\left\{u'^{(2\omega)}_{mn}, v'^{(2\omega)}_{mn}\right\}$, $\left\{u''^{(2\omega)}_{mn}, v''^{(2\omega)}_{mn}\right\}$

The coefficients $\left\{u'^{(2\omega)}_{mn}, v'^{(2\omega)}_{mn}\right\}$ for the surface tangential source can be expressed as:

$$u'^{(2\omega)}_{mn} = i2\frac{\zeta_e}{\zeta_0}\sum_{n_1}^{\infty}\sum_{m_1=-n_1}^{n_1}\sum_{n_2}^{\infty}\sum_{m_2=-n_2}^{n_2} A^{(1)}_{m_1n_1}A^{(-1)}_{m_2n_2}C^{(1,0,-1)}_{n_1m_1n_2m_2nm} + A^{(0)}_{m_1n_1}A^{(-1)}_{m_2n_2}C^{(1,1,-1)}_{n_1m_1n_2m_2nm}$$

$$v'^{(2\omega)}_{mn} = -2\frac{\zeta_e}{\zeta_0}\sum_{n_1}^{\infty}\sum_{m_1=-n_1}^{n_1}\sum_{n_2}^{\infty}\sum_{m_2=-n_2}^{n_2} A^{(1)}_{m_1n_1}A^{(-1)}_{m_2n_2}C^{(0,0,-1)}_{n_1m_1n_2m_2nm} + A^{(0)}_{m_1n_1}A^{(-1)}_{m_2n_2}C^{(0,1,-1)}_{n_1m_1n_2m_2nm}$$

where

$$\begin{aligned} A^{(0)}_{mn} &= j_n(k_i(\omega)r)|_{r=R}\, c^{(\omega)}_{mn} \\ A^{(1)}_{mn} &= i\frac{1}{k_i(\omega)}\left(\frac{\partial}{\partial r} + \frac{1}{r}\right) j_n\left(k_i(\omega)r\right)\Big|_{r=R} d^{(\omega)}_{mn} \\ A^{(-1)}_{mn} &= i\sqrt{n(n+1)}\frac{1}{k_i(\omega)r}\, j_n\left(k_i(\omega)r\right)\Big|_{r=R} d^{(\omega)}_{mn} \end{aligned}$$

$$
\begin{aligned}
&C^{(0,1,-1)}_{J_1M_1J_2M_2JM} = \sqrt{\frac{3}{2\pi}}C^{JM}_{J_1M_1J_2M_2}\cdot \\
&\Bigg[\sqrt{(J_1+1)(J_2)(2J_1-1)(2J_2-1)}\begin{Bmatrix} J_1 & J_1-1 & 1 \\ J_2 & J_2-1 & 1 \\ J & J & 1 \end{Bmatrix} C^{J0}_{(J_1-1)(0)(J_2-1)(0)} \\
&-\sqrt{(J_1+1)(J_2+1)(2J_1-1)(2J_2+3)}\begin{Bmatrix} J_1 & J_1-1 & 1 \\ J_2 & J_2+1 & 1 \\ J & J & 1 \end{Bmatrix} C^{J0}_{(J_1-1)(0)(J_2+1)(0)} \\
&+\sqrt{(J_1)(J_2)(2J_1+3)(2J_2-1)}\begin{Bmatrix} J_1 & J_1+1 & 1 \\ J_2 & J_2-1 & 1 \\ J & J & 1 \end{Bmatrix} C^{J0}_{(J_1+1)(0)(J_2-1)(0)} \\
&-\sqrt{(J_1)(J_2+1)(2J_1+3)(2J_2+3)}\begin{Bmatrix} J_1 & J_1+1 & 1 \\ J_2 & J_2+1 & 1 \\ J & J & 1 \end{Bmatrix} C^{J0}_{(J_1+1)(0)(J_2+1)(0)}\Bigg]
\end{aligned}
$$

$$
\begin{aligned}
&C^{(1,0,-1)}_{J_1M_1J_2M_2JM} = \sqrt{\frac{3}{2\pi}}(2J_1+1)C^{JM}_{J_1M_1J_2M_2}\cdot \\
&\Bigg[\sqrt{(J_2)(2J_2-1)}\begin{Bmatrix} J_1 & J_1 & 1 \\ J_2 & J_2-1 & 1 \\ J & J+1 & 1 \end{Bmatrix} C^{(J+1)0}_{(J_1)(0)(J_2-1)(0)}\sqrt{\frac{J}{2J+1}} \\
&-\sqrt{(J_2+1)(2J_2+3)}\ \begin{Bmatrix} J_1 & J_1 & 1 \\ J_2 & J_2+1 & 1 \\ J & J+1 & 1 \end{Bmatrix} C^{(J+1)0}_{(J_1)(0)(J_2+1)(0)}\sqrt{\frac{J}{2J+1}} \\
&+\sqrt{(J_2)(2J_2-1)}\begin{Bmatrix} J_1 & J_1 & 1 \\ J_2 & J_2-1 & 1 \\ J & J-1 & 1 \end{Bmatrix} C^{(J-1)0}_{(J_1)(0)(J_2-1)(0)}\sqrt{\frac{J+1}{2J+1}} \\
&-\sqrt{(J_2+1)(2J_2+3)}\ \begin{Bmatrix} J_1 & J_1 & 1 \\ J_2 & J_2+1 & 1 \\ J & J-1 & 1 \end{Bmatrix} C^{(J-1)0}_{(J_1)(0)(J_2+1)(0)}\sqrt{\frac{J+1}{2J+1}}\Bigg]
\end{aligned}
$$

$$
\begin{aligned}
&C^{(0,0,-1)}_{J_1M_1J_2M_2JM} = \sqrt{\frac{3}{2\pi}}(2J_1+1)C^{JM}_{J_1M_1J_2M_2}\cdot \\
&\Bigg[\sqrt{(J_2)(2J_2-1)}\begin{Bmatrix} J_1 & J_1 & 1 \\ J_2 & J_2-1 & 1 \\ J & J & 1 \end{Bmatrix} C^{J0}_{(J_1)(0)(J_2-1)(0)}\ -\sqrt{(J_2+1)(2J_2+3)}\begin{Bmatrix} J_1 & J_1 & 1 \\ J_2 & J_2+1 & 1 \\ J & J & 1 \end{Bmatrix} C^{J0}_{(J_1)(0)(J_2+1)(0)}\Bigg]
\end{aligned}
$$

$$
\begin{aligned}
&C^{(1,1,-1)}_{J_1M_1J_2M_2JM} = \sqrt{\frac{3}{2\pi}} C^{JM}_{J_1M_1J_2M_2} \cdot \\
&\Bigg[\sqrt{(J_1+1)(J_2)(2J_1-1)(2J_2-1)} \left\{ \begin{matrix} J_1 & J_1-1 & 1 \\ J_2 & J_2-1 & 1 \\ J & J+1 & 1 \end{matrix} \right\} C^{(J+1)0}_{(J_1-1)(0)(J_2-1)(0)} \sqrt{\frac{J}{2J+1}} \\
&-\sqrt{(J_1+1)(J_2+1)(2J_1-1)(2J_2+3)} \left\{ \begin{matrix} J_1 & J_1-1 & 1 \\ J_2 & J_2+1 & 1 \\ J & J+1 & 1 \end{matrix} \right\} C^{(J+1)0}_{(J_1-1)(0)(J_2+1)(0)} \sqrt{\frac{J}{2J+1}} \\
&+\sqrt{(J_1)(J_2)(2J_1+3)(2J_2-1)} \left\{ \begin{matrix} J_1 & J_1+1 & 1 \\ J_2 & J_2-1 & 1 \\ J & J+1 & 1 \end{matrix} \right\} C^{(J+1)0}_{(J_1+1)(0)(J_2-1)(0)} \sqrt{\frac{J}{2J+1}} \\
&-\sqrt{(J_1)(J_2+1)(2J_1+3)(2J_2+3)} \left\{ \begin{matrix} J_1 & J_1+1 & 1 \\ J_2 & J_2+1 & 1 \\ J & J+1 & 1 \end{matrix} \right\} C^{(J+1)0}_{(J_1+1)(0)(J_2+1)(0)} \sqrt{\frac{J}{2J+1}} \\
&+\sqrt{(J_1+1)(J_2)(2J_1-1)(2J_2-1)} \left\{ \begin{matrix} J_1 & J_1-1 & 1 \\ J_2 & J_2-1 & 1 \\ J & J-1 & 1 \end{matrix} \right\} C^{(J-1)0}_{(J_1-1)(0)(J_2-1)(0)} \sqrt{\frac{J+1}{2J+1}} \\
&-\sqrt{(J_1+1)(J_2+1)(2J_1-1)(2J_2+3)} \left\{ \begin{matrix} J_1 & J_1-1 & 1 \\ J_2 & J_2+1 & 1 \\ J & J-1 & 1 \end{matrix} \right\} C^{(J-1)0}_{(J_1-1)(0)(J_2+1)(0)} \sqrt{\frac{J+1}{2J+1}} \\
&+\sqrt{(J_1)(J_2)(2J_1+3)(2J_2-1)} \left\{ \begin{matrix} J_1 & J_1+1 & 1 \\ J_2 & J_2-1 & 1 \\ J & J-1 & 1 \end{matrix} \right\} C^{(J-1)0}_{(J_1+1)(0)(J_2-1)(0)} \sqrt{\frac{J+1}{2J+1}} \\
&-\sqrt{(J_1)(J_2+1)(2J_1+3)(2J_2+3)} \left\{ \begin{matrix} J_1 & J_1+1 & 1 \\ J_2 & J_2+1 & 1 \\ J & J-1 & 1 \end{matrix} \right\} C^{(J-1)0}_{(J_1+1)(0)(J_2+1)(0)} \sqrt{\frac{J+1}{2J+1}} \Bigg]
\end{aligned}
$$

where $C^{JM}_{J_1M_1J_2M_2}$ are the Clebsch-Gordan coefficients [Chapter 8 in Ref. 21], and the quantities in braces are Wigner $6j$ and $9j$ symbols [Chapters 9 and 10 in Ref. 21].

The coefficients $\left\{ u''^{(2\omega)}_{mn}, v''^{(2\omega)}_{mn} \right\}$ for both the bulk and the surface normal polarization source can be expressed as:

$$
\begin{aligned}
u''^{(2\omega)}_{mn} &= i\sqrt{n(n+1)} \frac{g_{mn}(k_i(\omega)R)}{k_0(\omega)R} + \frac{\varepsilon_0}{\varepsilon_i(2\omega)} i\sqrt{n(n+1)} \frac{f_{mn}(k_i(\omega)R)}{k_0(\omega)R} \\
v''^{(2\omega)}_{mn} &= 0
\end{aligned}
$$

where

$$
\begin{aligned}
&g_{mn}(k_i(\omega)R) = \sum_{n_1m_1} \sum_{n_2m_2} \\
&\Bigg\{ A^{(-1)}_{m_1n_1} A^{(-1)}_{m_2n_2} \left[\sqrt{\frac{n_1}{2n_1+1}} \sqrt{\frac{n_2}{2n_2+1}} W^{n_1-1,n_1,m_1,n_2-1,n_2,m_2}_{nm} + \sqrt{\frac{n_1+1}{2n_1+1}} \sqrt{\frac{n_2+1}{2n_2+1}} W^{n_1+1,n_1,m_1,n_2+1,n_2,m_2}_{nm} \right] \\
&-A^{(-1)}_{m_1n_1} A^{(-1)}_{m_2n_2} \left[\sqrt{\frac{n_1}{2n_1+1}} \sqrt{\frac{n_2+1}{2n_2+1}} W^{n_1-1,n_1,m_1,n_2+1,n_2,m_2}_{nm} + \sqrt{\frac{n_1+1}{2n_1+1}} \sqrt{\frac{n_2}{2n_2+1}} W^{n_1+1,n_1,m_1,n_2-1,n_2,m_2}_{nm} \right] \Bigg\}
\end{aligned}
$$

$$
\begin{aligned}
&f_{mn}(k_i(\omega)R) = \sum_{n_1,m_1}\sum_{n_2,m_2} \\
&\Bigg\{A^{(1)}_{m_1n_1}A^{(1)}_{m_2n_2}\left[\sqrt{\frac{n_1+1}{2n_1+1}}\sqrt{\frac{n_2+1}{2n_2+1}}W_{nm}^{n_1-1,n_1,m_1,n_2-1,n_2,m_2}+\sqrt{\frac{n_1}{2n_1+1}}\sqrt{\frac{n_2}{2n_2+1}}W_{nm}^{n_1+1,n_1,m_1,n_2+1,n_2,m_2}\right] \\
&+A^{(1)}_{m_1n_1}A^{(1)}_{m_2n_2}\left[\sqrt{\frac{n_1+1}{2n_1+1}}\sqrt{\frac{n_2}{2n_2+1}}W_{nm}^{n_1-1,n_1,m_1,n_2+1,n_2,m_2}+\sqrt{\frac{n_1}{2n_1+1}}\sqrt{\frac{n_2+1}{2n_2+1}}W_{nm}^{n_1+1,n_1,m_1,n_2-1,n_2,m_2}\right] \\
&+A^{(0)}_{m_1n_1}A^{(0)}_{m_2n_2}\ W_{nm}^{n_1,n_1,m_1,n_2,n_2,m_2} \\
&+A^{(-1)}_{m_1n_1}A^{(-1)}_{m_2n_2}\left[\sqrt{\frac{n_1}{2n_1+1}}\sqrt{\frac{n_2}{2n_2+1}}W_{nm}^{n_1-1,n_1,m_1,n_2-1,n_2,m_2}+\sqrt{\frac{n_1+1}{2n_1+1}}\sqrt{\frac{n_2+1}{2n_2+1}}W_{nm}^{n_1+1,n_1,m_1,n_2+1,n_2,m_2}\right] \\
&-A^{(-1)}_{m_1n_1}A^{(-1)}_{m_2n_2}\left[\sqrt{\frac{n_1}{2n_1+1}}\sqrt{\frac{n_2+1}{2n_2+1}}W_{nm}^{n_1-1,n_1,m_1,n_2+1,n_2,m_2}+\sqrt{\frac{n_1+1}{2n_1+1}}\sqrt{\frac{n_2}{2n_2+1}}W_{nm}^{n_1+1,n_1,m_1,n_2-1,n_2,m_2}\right] \\
&+A^{(1)}_{m_1n_1}A^{(0)}_{m_2n_2}\left[\sqrt{\frac{n_1+1}{2n_1+1}}W_{nm}^{n_1-1,n_1,m_1,n_2,n_2,m_2}+\sqrt{\frac{n_1}{2n_1+1}}W_{nm}^{n_1+1,n_1,m_1,n_2,n_2,m_2}\right] \\
&+A^{(0)}_{m_1n_1}A^{(1)}_{m_2n_2}\left[\sqrt{\frac{n_2+1}{2n_2+1}}W_{nm}^{n_1,n_1,m_1,n_2-1,n_2,m_2}+\sqrt{\frac{n_2}{2n_2+1}}W_{nm}^{n_1,n_1,m_1,n_2+1,n_2,m_2}\right]\Bigg\}
\end{aligned}
$$

$$
W_{LM}^{L1,J1,M1,L2,J2,M2} = (-1)^{J_2+L_1+L}\sqrt{\frac{(2J_1+1)(2J_2+1)(2L_1+1)(2L_2+1)}{4\pi(2L+1)}}\begin{Bmatrix} L_1 & L_2 & L \\ J_2 & J_1 & 1 \end{Bmatrix} C^{L0}_{L_10L_20}\,C^{LM}_{J_1M_1J_2M_2}
$$

ACKNOWLEDGMENTS

This work was partly supported by the Italian Miur through the project PON01-02782. L.D.N. acknowledges the support of the NSF Career Award No. ECCS-0846651.

---

[*] Corresponding author: miano@unina.it

[1] H. Aouani, M. Navarro-Cia, M. Rahmani, T. P. H. Sidiropoulos, M. Hong, R. F. Oulton, and S. A. Maier, Nano Letters **12**, 4997 (2012).

[2] J. Butet, J. Duboisset, G. Bachelier, I. Russier-Antoine, E. Benichou, C. Jonin, and P.-F. Brevet, Nano Letters **10**, 1717 (2010).

[3] A. Capretti, G. F. Walsh, S. Minissale, J. Trevino, C. Forestiere, G. Miano, and L. D. Negro, Opt. Express **20**, 15797 (2012).

[4] C. G. Biris and N. C. Panoiu, Phys. Rev. B **81**, 195102 (2010).

[5] L. Tong and J. Cheng, Materials Today **14**, 264 (2011).

[6] G. Gonella and H.-L. Dai, Phys. Rev. B **84**, 121402 (2011).

[7] T. Heinz, "Second-order nonlinear optical effects at surfaces and interfaces," in *Nonlinear surface electromagnetic phenomena*, Modern problems in condensed matter sciences, edited by H. Ponath and G. Stegeman (North-Holland, 1991) pp. 353–416.

[8] G. Agarwal and S. Jha, Solid State Communications **41**, 499 (1982).

[9] J. I. Dadap, J. Shan, K. B. Eisenthal, and T. F. Heinz, Phys. Rev. Lett. **83**, 4045 (1999).

[10] P. Guyot-Sionnest, W. Chen, and Y. R. Shen, Phys. Rev. B **33**, 8254 (1986).

[11] P. Guyot-Sionnest and Y. R. Shen, Phys. Rev. B **35**, 4420 (1987).

[12] V. L. Brudny, B. S. Mendoza, and W. Luis Mochán, Phys. Rev. B **62**, 11152 (2000).

[13] J. I. Dadap, J. Shan, and T. F. Heinz, J. Opt. Soc. Am. B **21**, 1328 (2004).

[14] Y. Pavlyukh and W. Hübner, Phys. Rev. B **70**, 245434 (2004).

[15] J. Xu and X. Zhang, Opt. Express **20**, 1668 (2012).

[16] F. X. Wang, F. J. Rodriguez, W. M. Albers, R. Ahorinta, J. E. Sipe, and M. Kauranen, Phys. Rev. B **80**, 233402 (2009).

[17] G. Bachelier, J. Butet, I. Russier-Antoine, C. Jonin, E. Benichou, and P.-F. Brevet, Phys. Rev. B **82**, 235403 (2010).

[18] J. Rudnick and E. A. Stern, Phys. Rev. B **4**, 4274 (1971).

[19] J. E. Sipe, V. C. Y. So, M. Fukui, and G. I. Stegeman,

Phys. Rev. B **21**, 4389 (1980).

[20] J. Jackson, *Classical Electrodynamics* (Wiley, 1998).

[21] D. Varshalovich, A. Moskalev, and V. Khersonski, *Quantum Theory of Angular Momentum* (World Scientific Pub., 1988).

[22] P. B. Johnson and R. W. Christy, Phys. Rev. B **6**, 4370 (1972).

[23] G. Gonella, W. Gan, B. Xu, and H.-L. Dai, The Journal of Physical Chemistry Letters **3**, 2877 (2012).

[24] R. Almeida, C. Barrios, R. Panepucci, and M. Lipson, Nature **431**, 1081 (2004).